Gibbs elasticity effect in foam shear flows: a non quasi-static 2D numerical simulation

I. Cantat*

Received 9th July 2010, Accepted 8th September 2010
DOI: 10.1039/c0sm00657b

The origin of the dissipation in liquid foams is not fully understood, especially in the large deformation, large velocity regime. Numerical simulations, now very accurate in the quasi static regime, are still sparse in the dissipative regime, and are all based on restrictive assumptions or very small bubble numbers. Here we present the results obtained with 2D numerical simulations involving 500 bubbles under simple shear, in a non-quasi static regime. The bubble description is kept as simple as possible and the dissipation is assumed to arise from surface tension variations induced by film area variations. This model leads to a steady state stress under simple shear that is well fitted by a Herschel–Bulkley law with an exponent 0.6. We show that small tension dynamical inhomogeneities induce foam structure modifications responsible for the largest part of the stress increase.

1 Introduction

A liquid foam is a good example of a visco-elasto-plastic material.[1–3] Extensive studies have been devoted to the elasto-plastic behavior in the quasi-static regime, which main features are now well understood (see ref. 1 for a review). In contrast, the origin of the stress variation with increasing shear rate is still the subject of an active debate. Experimentally, the flow at constant shear rate is well described by the Herschel–Bulkley law $\sigma = \sigma_y + k\dot{\varepsilon}^n$, with n an exponent smaller than unity, σ_y the yield stress and $\dot{\varepsilon}$ the shear rate.[4–7] Several models predict this shear thinning behavior, using very different approaches. The SGR model,[8,9] the mode coupling theory[10] and the KEP model[11] all consider that energy dissipation only occurs during short plastic events and that the stress is of purely elastic nature. The shear rate dependency arises because the system can spend some time above the quasi static yield stress. At high shear rates, the material can thus reach higher deformations than at low shear rate. The KEP model predicts $n = 1/2$, without assuming any local nonlinearity in the dissipation law.[11] In contrast, Denkov *et al.* assume that friction occurs continuously because of the bubble/bubble relative motion and that the $n = 1/2$ value can be obtained by computation at the bubble scale.[12,13] In that model, bubble elongation does not increase with increasing shear rate. This second model allows for a quantitative agreement with experimental data, and thus probably captures the main physical processes, for soluble and highly mobile surfactants and intermediate liquid fractions (ϕ_l around 0.1). Using insoluble surfactants, Denkov *et al.* show that the power law is modified and that $n \approx 0.25$, which origin is not entirely elucidated. The disorder, governed by the bubble size distribution, also plays an important role.[14] The bubble motion induces local interface stretching or compression, variation of surfactant concentration at the interface and finally surface tension modification. Solving the full surfactants dynamics would require to solve a coupled problem involving the hydrodynamics equations and the diffusion equations both in the fluid phase (with free boundaries) and in the interface. This is still numerically out of reach, but simplified models can be enlightening. Pozrikidis solved the problem for a large fluid fraction and totally insoluble surfactants, for few tens of bubbles, in two dimensions.[15] In this paper we focus on 2D very dry foams and we assume that the dynamics are limited by the surfactant adsorption and desorption. We show that this simple model predicts a Herschel–Bulkley behavior with $n \approx 0.6$. The stress increase is mainly due to an increase of the bubble deformation with the shear rate, as already observed on a periodic hexagonal structure by Kraynik and Hansen.[16] The bubble model, which takes into account a very different source of dissipation, leads to $n \approx 0.5$.[17] In both cases, the forces vary linearly with the shear rate at the bubble scale. The second and third sections of the paper are devoted respectively to the general presentation of the model and to its numerical discretization. We present our numerical results in section 4 and discuss them in section 5.

IPR, UMR CNRS 6251, Université Rennes 1, bât 11A, campus de Beaulieu, 35042 Rennes cedex, France. E-mail: isabelle.cantat@univ-rennes1.fr

2 Modeling of the flow

2.1 Two dimensional foam

We consider a single layer of bubbles submitted to a simple shear deformation, at constant shear rate (in the layer plane). Dissipation in foam may occur through multiple processes that were first discussed by Buzza and Cates.[18] These local processes may be classified in two classes: those involving the bulk viscosity and those involving surfactant properties (viscosity or diffusivity). Here we assume that the slowest process is the surfactant concentration relaxation: at each time the foam structure is at mechanical equilibrium under the effect of out of equilibrium surface tension. This has been proved to be the limiting factor for the bubble relaxation after a T1 transformation.[19] In contrast with our previous work,[20] it is assumed here that the internal dissipation, due to the relative motion of the bubbles, dominates and that any external dissipation, due to a friction on walls for example, is negligible. The focus is on the dry regime limit and the Plateau borders have negligible sizes.

2.2 Surface tension and surfactant concentration

In our model, the evolution of the surfactant concentration at the interface $\tilde{\Gamma}$ is limited by an adsorption/desorption characteristic time τ (the $\tilde{\cdot}$ indicates a dimensioned variable). This is the only internal time we put in the model, so it directly controls the shear rate at which the quasi static regime ends. It may be seen as the real microscopic time related to the adsorption/desorption mechanism, or as an effective time scale related to the surfactant exchange with the bulk, limited by the diffusion. If the second mechanism is the dominant one, the model is only a crude approximation and the full diffusion field would need to be solved. Finally, the concentration is assumed to be uniform on each edge and the surfactant exchange between adjacent edges is neglected. The surfactant mass balance thus leads to the relation, with $\tilde{\mathcal{L}}$ the curvilinear edge length

$$\frac{d\tilde{\Gamma}}{d\tilde{t}} = \frac{1}{\tau}\left(\tilde{\Gamma}_{eq} - \tilde{\Gamma}\right) - \frac{\tilde{\Gamma}}{\tilde{\mathcal{L}}}\frac{d\tilde{\mathcal{L}}}{d\tilde{t}} \tag{1}$$

For sake of simplicity, a linear relation is used between the concentration $\tilde{\Gamma}$ and the surface tension $\tilde{\gamma}$:

$$\tilde{\gamma} = \tilde{\gamma}_{eq} - E\frac{\tilde{\Gamma} - \tilde{\Gamma}_{eq}}{\tilde{\Gamma}_{eq}} \tag{2}$$

where E is the high frequency dilatational elastic surface modulus.

2.3 Dimensionless equations

Using the internal surfactant exchange time τ, the equilibrium surface tension γ_{eq} and the equilibrium surface concentration Γ_{eq} as time, force and concentration units, we get the dimensionless set of equations

$$\gamma = 1 - \alpha(\Gamma - 1) \tag{3}$$

$$\frac{d\Gamma}{dt} = (1 - \Gamma) - \frac{\Gamma}{\mathcal{L}}\frac{d\mathcal{L}}{dt} \tag{4}$$

$$\frac{d\gamma}{dt} = (1 - \gamma) - \frac{(\gamma - (1 + \alpha))}{\mathcal{L}}\frac{d\mathcal{L}}{dt} \tag{5}$$

with $\alpha = E/\gamma_{eq}$. This parameter has been set to 1 in the presented results. The unit length chosen for the simulations is the box size.

3 Numerical simulation

Our numerical solution is based on the vertex model.[21,20] In this model, the 2D foam is represented by a set of polygons tiling the plane: each vertex i is connected to three vertices j, with $j \in \mathcal{J}_i$, by an edge (ij). At equilibrium, the edges between two bubbles in a 2D foam structure are part of circles. However, there is no reason for this feature to remain valid in an out of equilibrium foam, so we chose the most simple representation, *i.e.* straight edges. The dynamical parameters are the vertices locations $\mathbf{r}_i = (x_i, y_i)$, the connectivity of the vertices network $\mathcal{J}_i$ and the surface tension γ_{ij} of the edge (ij). The subsystem S_i is made of the vertex i with its three outgoing edges reduced by half, as depicted on Fig. 1. At each time step, the new structure, corresponding to the imposed shear ε, is determined by a (not physical) relaxation process. At the end of this relaxation loop presented below, the surface tensions γ_{ij} have non equilibrium values, but the total force exerted on each subsystem S_i is smaller than ε_F, an arbitrarily small cut off. This is in agreement with the assumption that the surfactant dynamics is the slowest process of the foam dynamics.

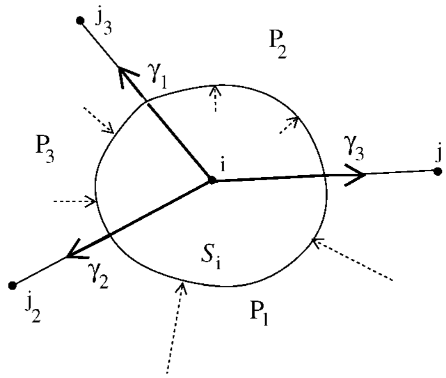

Fig. 1 Definition of the subsystem S_i, and forces acting on it.

3.1 Initial condition

The simulation is made in a biperiodic square box of surface unity. A Voronoi tessellation first allows one to build a disordered structure. A target area $A_{k,0}$ is chosen randomly for each bubble k with the law $A_{k,0} = \langle A\rangle(0.38 + 1.24x_{ran})$, x_{ran} being a random number equally distributed between 0 and 1. This target area is kept constant, as coarsening or bubble coalescence is disregarded. The actual area of each bubble always remains close to this target value, as discussed below, and the value of $\mu_2(A) = \langle A^2\rangle/\langle A\rangle^2 - 1$ is close to 0.12. The structure is then relaxed toward an equilibrium foam structure (with equilibrium surface tensions) using the relaxation loop detailed in the next paragraph. Each periodic box has an index (I,J). The connectivity of the vertex i is given by the list of three vertices $j_1(i)$,$j_2(i)$,$j_3(i)$, with the indication of the periodic box they belong to (see Fig. 2).

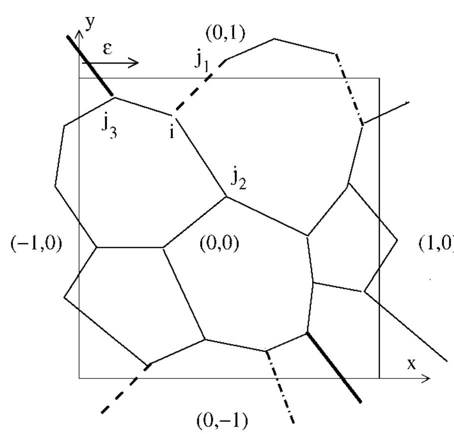

Fig. 2 Example of biperiodic foam with few bubbles. The shear deformation ε is given by the arrow. The edges with the same kind of line (thick, dashed or dotted dashed) are periodic images of each other, in different periodic boxes labelled by (I,J).

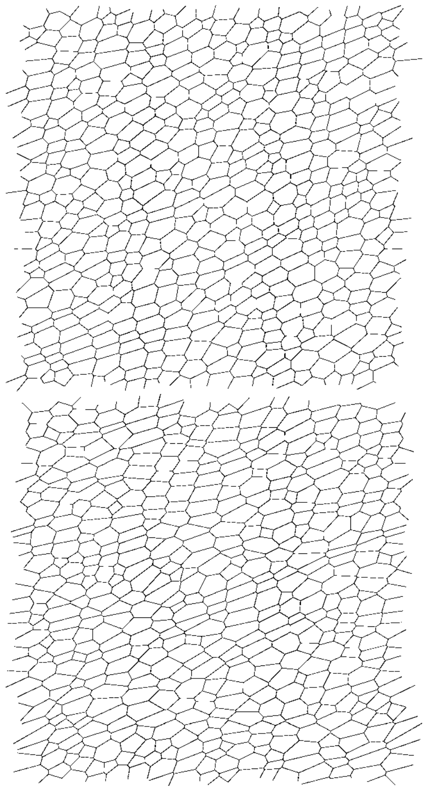

Fig. 3 Foam structures obtained in the steady state for $\dot{\varepsilon} = 10^{-3}$ (upper) and $\dot{\varepsilon} = 4 \times 10^{-2}$ (lower)(reduced units). The upper boundary moves to the right.

3.2 Shearing a biperiodic structure

We want to impose a shear without solid boundary. This is achieved by translating the periodic boxes with the rule $X(I,J) = I + \varepsilon J$, $Y(I,J) = J$, (X,Y) being the position of the lower left corner of the box. This induces an imposed shear of amplitude ε in the x direction, with the velocity gradient oriented in the y direction (see fig. 2). If the vertex j has the reference position (x,y) in the box (0,0) but belongs to the box (I,J), its actual position is $(x + I + \varepsilon J, y + J)$. This allows to compute the edge lengths between vertices belonging to different boxes.

3.3 Shear and relaxation loop

In order to compute the foam structure at time $t + \delta t$, a global shear increment $\delta\varepsilon$ is imposed to the system. A guessed position (x_i^0, y_i^0) is chosen for each vertex i with the law $x_i^0 = x_i(t) + \delta\varepsilon y_i(t)$, $y_i^0 = y_i(t)$. Each vertex then follows the direction of the total force exerted on the subsystem S_i, until the maximal force exerted on a subsystem becomes smaller than the chosen precision ε_F. Below, the subscript n denotes the non physical values obtained after n iterations of the relaxation loop.

At the step n, the tension force is, with $\mathbf{r}_{ij}^n = \mathbf{r}_i^n - \mathbf{r}_j^n$ and $r_{ij}^n = \|r_i^n - \mathbf{r}_j^n\|$,

$$\mathbf{F}_{t,i}^n = \sum_{j \in \mathcal{J}_i} \gamma_{ij}^n \frac{\mathbf{r}_{ij}^n}{r_{ij}^n} \tag{6}$$

where the surface tension γ_{ij}^n is obtained from eqn (5), using $\alpha = 1$:

$$\gamma_{ij}^n = \gamma_{ij}(t) + \left(1 - \gamma_{ij}(t)\right)dt - \left(\gamma_{ij}(t) - 2\right)\frac{r_{ij}^n - r_{ij}(t)}{r_{ij}(t)} \tag{7}$$

$\gamma_{ij}(t)$ and $r_{ij}(t)$ are respectively the surface tension of the edge (ij) and its length in the previous relaxed structure, at time t.

With $\mathbf{n}_{ij}$, the normal to the edge (ij), oriented arbitrarily, say from a bubble k towards a bubble k' and with $\delta P_{ij} = P_{k'} - P_k$ the pressure gap on this edge, the pressure force exerted on S_i is:

$$\mathbf{F}_{p,i}^n = -\sum_{j \in \mathcal{J}_i} \frac{r_{ij}^n}{2} \delta P_{ij}^n \mathbf{n}_{ij}^n \tag{8}$$

The 1/2 factor just arises from the system definition (see Fig. 1). The pressure in the bubble k is given, at the step n, by

$$P_k^n = -\lambda \frac{A_k^n - A_{k,0}}{A_{k,0}} \tag{9}$$

with A_k^n the actual area of the bubble k at the step n and $A_{k,0}$ its target area. The constant λ is the foam numerical compressibility: it is devoid of physical meaning and it is chosen large enough to keep the area relative variation small, and small enough to ensure the numerical stability.

At each step n the position $\mathbf{r}_i^n$ becomes $\mathbf{r}_i^{n+1} = \mathbf{r}_i^n + \delta\mathbf{r}_i^n$, with $\delta\mathbf{r}_i^n$ proportional to the force exerted on S_i: $\mathbf{F}_i^n = \mathbf{F}_{t,i}^n + \mathbf{F}_{p,i}^n$. We obtained stable results using $\delta\mathbf{r}_i^n = 10^{-3}\mathbf{F}_i^n$. If an edge becomes smaller than a given cut off ε_l, a T1 event is performed, modifying the connectivity network of the foam. The new edge is built perpendicularly to the disappearing one, with an initial length of $1.3\varepsilon_l$. The relaxation loop ended at the step n_{max} when, on each vertex, the total force $\|\mathbf{F}_i^n\|$ is smaller than a chosen value ε_F. The vertices positions and edges tensions at the new time $t + dt$ are then given by the values of $\mathbf{r}_i^{n_{max}}$ and $\gamma_{ij}^{n_{max}}$.

3.4 Parameters and robustness of the simulation

All the simulations have been performed with $N = 500$ bubbles. Their average area is thus $\langle A \rangle = 0.002$ and their typical length scale $l_b = \sqrt{\langle A \rangle} = 0.045$. The compressibility factor $\lambda = 8/l_b = 177$ is large enough to ensure that $\delta A/A < 10\%$. The results presented in the next section do not depend notably on this parameter. The relaxation process ends when the maximal residual force on a vertex becomes lower than $\varepsilon_F F_{\mathrm{ref}}$ with $\varepsilon_F = 0.0002$ and F_{ref} a reference force corresponding to a vertex with an angle of π/2 between two edges and equilibrium tensions. The smallest edge length before doing a T1 is $\varepsilon_l = 0.08 l_b = 0.0036$. This parameter gives the 2D liquid fraction of the foam:[22]

$$\phi = \frac{1}{\langle A \rangle}\left(\sqrt{3} - \frac{\pi}{2}\right)\frac{3}{2}\varepsilon_l^2 = 10^{-3} \tag{10}$$

It strongly affects the yield deformation and must be considered as a physical parameter, in contrast with the other purely numerical quantities. We chose its value to deal with the limit of very dry foam.

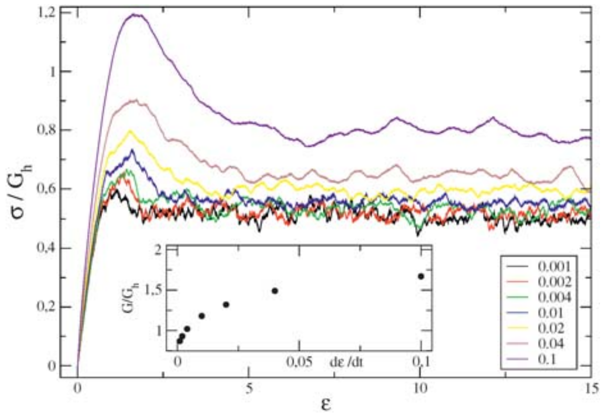

Fig. 4 Average stress in the sample, normalised by the elastic shear modulus of the honeycomb foam of same average bubble area G_h, as a function of the shear, for different shear rate values, listed in the legend. Inset: elastic shear modulus obtained from the same data, by linear fit of the curves in the domain $\varepsilon < 0.1$.

4 Shear start up simulation

The foam is at equilibrium at $t = 0$ and a simple shear is imposed for $t > 0$. The main control parameter is the shear rate that has been varied between 10^{-3} and 10^{-1} (in reduced units, see section 2.3). Higher shear rates lead to numerical instabilities, and lower shear rates do not provide new information, as $\dot{\varepsilon} = 10^{-3}$ is already in the quasi static regime. No shear banding has been observed in the simulations.

4.1 Shear modulus and overshoot

The average stress value in the sample is computed using the Batchelor expression

$$\sigma_{lm} = \frac{1}{2}\sum_{i,j\in\mathcal{J}_i}\gamma_{ij}\frac{r_{ij,l}r_{ij,m}}{r_{ij}} - \sum_k P_k A_k \delta_{lm} \quad (11)$$

where l and m represent the x or y directions. The stress $\sigma = \sigma_{xy}$ is reported as a function of ε for various shear rates on Fig. 4. It is normalized by the quasi static shear modulus of a hexagonal network with the same average bubble area: $G_h = 0.26\gamma\sqrt{\pi}/\sqrt{\langle A_h\rangle}$, with γ the surface tension of the film (*i.e.* twice the interfacial surface tension) and A_h the average area of the hexagons.[23] With our parameters, $\sqrt{\langle A_h\rangle} = 0.045$ and $\gamma = 1$ (see section 3.4), so $G_h = 10.3$.

The quasi static shear modulus, obtained by a linear fit of the curve $\sigma(\varepsilon)$ in the region $\varepsilon < 0.1$ for $\dot{\varepsilon} = 10^{-3}$, is $G_{QS} = 0.87G_h$ (see Fig. 4, inset). This value is in agreement with the Surface Evolver Simulation made on 2D disordered foam having the same polydispersity ($\mu_2(A) \approx 0.1$[24]). The out of equilibrium surface tension induces visco-elasticity at small deformation. The shear modulus G, defined here as the slope σ/ε at small deformation, increases with the shear rate, as depicted on the inset of Fig. 4.

The highest stress value σ_{max} reached by the system increases rapidly with the shear rate. This is mainly due to the fact that the dissipation delays the onset of T1s. This has also been observed by Green *et al.* with another source of dissipation.[25] The stress then decreases at the end of the transient, as T1s begin to occur and to relax the structure. The stress overshoot σ_{max}/σ_{SS} obtained between the elastic regime and the steady state (SS) potentially contributes to the phenomenon of shear banding in foam.[26] It is already present in the quasi static regime ($\sigma_{max}/\sigma_{SS} = 1.1$ for $\dot{\varepsilon} = 10^{-3}$), as observed by Surface Evolver simulations,[27] but it is much more pronounced at high shear rates ($\sigma_{max}/\sigma_{SS} = 1.6$ for $\dot{\varepsilon} = 10^{-1}$).

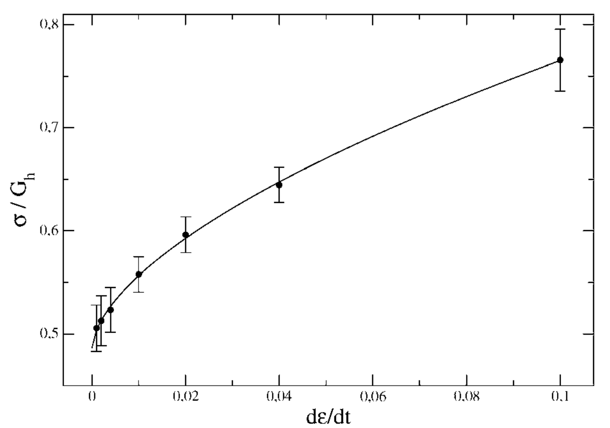

Fig. 5 Steady state value of the stress, normalised by G_h, as a function of the shear rate, obtained by averaging the data of Fig.4 in the steady state. The error bars represent the mean square value of the data. The full line is the best Herschel–Bulkley law, given in the text.

4.2 Stress in steady state

For deformations larger than few unities, the stress relaxes toward a steady value, given on Fig. 5. The data are well fitted by the Herschel–Bulkley law $\sigma/G_h = 0.48 + 1.10\dot{\varepsilon}^{0.6}$. The exponent is very sensitive to the yield stress value $\sigma_y = 0.48G_h$ and its error bar is thus of the order of ±0.1 (as well as for the other exponents given in the text).

For such visco-elasto-plastic materials, authors commonly try to identify the elastic and viscous contributions to the total stress. In our system, as the dissipation arises directly from the surface tension variation, *i.e.* from the quantity also responsible for the elastic response, this separation into two distinct contributions is far from obvious. We found it interesting to plot the shear stress that would be obtained with the same structure, but with the equilibrium surface tension on each edge. This artificial stress, denoted by σ_{str} is given by:

$$\sigma_{lm,str} = \frac{1}{2}\sum_{i,j\in\mathcal{J}_i}\frac{r_{ij,l}r_{ij,m}}{r_{ij}} - \sum_k P_k A_k \delta_{lm} \quad (12)$$

The value of $\sigma_{str} = \sigma_{xy,str}$, averaged over the whole steady state, is plotted on Fig. 6, as well as the difference $\delta\sigma = \sigma - \sigma_{str}$. An important result is that the largest part of the stress increase in the non quasi-static regime is due to an increase of the bubble deformation. The best power law fit for σ_{str} is $\sigma_{str} = \sigma_y + 0.64G_h\dot{\varepsilon}^{0.51}$. The surface tension variation thus has two contributions: (i) it increases the deformation reached by the bubble when the T1 occurs, which can be seen as an increase of the yield strain; (ii) the edges having a positive contribution to σ_{xy} (*i.e.* having an orientation $\theta \in [0,\pi/2]$) are, in average, stretched and thus have a larger tension than the edges with a negative contribution (*i.e.* having an orientation $\theta \in [\pi/2,\pi]$): this leads to

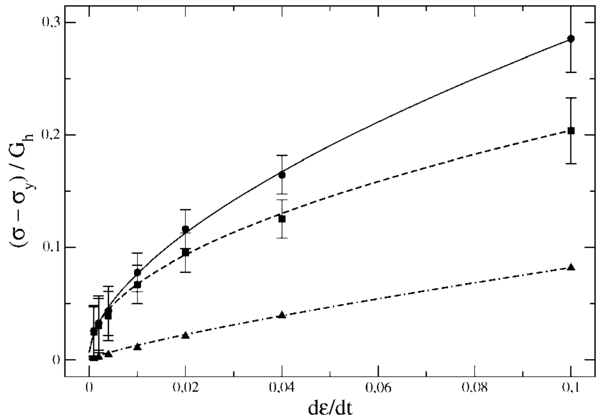

Fig. 6 •: $(\sigma - \sigma_y)/G_h$, same data as for Fig. 5. ■: $(\sigma_{str} - \sigma_y)/G_h$. ▲: $(\sigma - \sigma_{str})/G_h$. The lines are the best power law fits.

a net increase of the stress, for a given structure. This second contribution is measured by $\sigma - \sigma_{str}$, which best power law fit is $\sigma - \sigma_{str} = 0.53G_h\dot{\varepsilon}^{0.81}$. This second term is much smaller than σ_{str}, which is in agreement with the small variation of the surface tension with shear rate, always smaller than 15% (see Fig. 11).

4.3 Foam structure

As the foam structure is responsible for the largest part of the stress increase with $\dot{\varepsilon}$, it is important to provide a precise characterization of the structure evolution with $\dot{\varepsilon}$. We thus plot the angular distribution of the edge lengths (Fig. 7) and of the edge density (Fig. 8).

The bubbles are elongated by the shear flow, which induces a preferential orientation for the longest bubble edges. The other edges also have preferential orientation, governed by the long edge orientation and the constraint that angles between edges must remain close to π/3. The edges density is thus not isotropic, even if the foam is not crystallized.

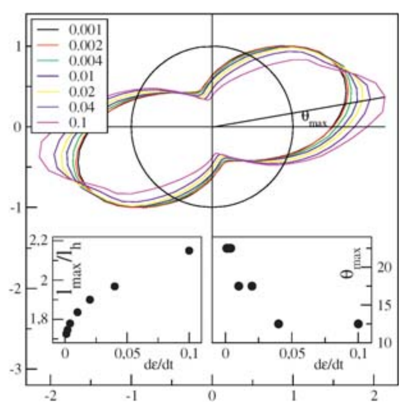

Fig. 7 Angular distribution of the edges lengths for shear rates in the range $10^{-3} - 10^{-1}$, in the steady state regime. The data binning has been made with $\delta\theta = 5°$. The lengths are rescaled by the edge length of the honeycomb structure $l_h = 0.028$. The circle represents the isotropic distribution. Insets (left): maximal edge length value. (right) direction of the longest edges.

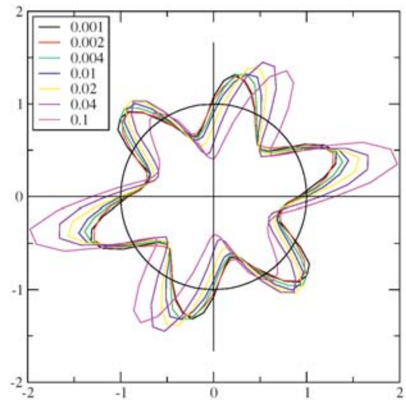

Fig. 8 Angular distribution of the edges density, for shear rates in the range $10^{-3} - 10^{-1}$, in the steady state regime. The data binning has been made with $\delta\theta = 5°$. The circle represents the isotropic distribution.

A synthetic way to characterize the foam deformation has been proposed by Graner *et al.*[28] The texture tensor M is built on the links between bubble centers $\mathbf{l}_{kk'}$:

$$M_{ij} = \langle l_{kk',i} l_{kk',j} \rangle_{k,k'} \tag{13}$$

For the honeycomb structure, the obtained value is $M_{h,ij} = A\delta_{ij}/\sqrt{3}$ with δ_{ij} the Kronecker symbol and A the hexagon's area. We thus set $M_0 = A/\sqrt{3}$ and plot the dimensionless values M_{ij}/M_0 on Fig. 9. The same thing can be done using the edges, instead of the adjacent bubble center links. For the edges the rescaling must be done with $M_{0,e} = A/(3\sqrt{3})$. Both tensors are similar, as depicted in Fig. 9 and we use the one built on links between bubble centers in the following. The square root of the rescaled eigenvalues, denoted by λ_1 and λ_2, and the direction of the eigenvectors of these tensors are plotted on Fig. 10, showing the elongation and the rotation induced by the shear. The elongation λ_1 and contraction λ_2 are fitted respectively by $\lambda_1 \sim 1.4 + 1.33\dot{\varepsilon}^{0.6}$ and $\lambda_2 \sim 0.76 - 0.37\dot{\varepsilon}^{0.5}$. The angular distribution of tensions (Fig. 11) shows moderate variations: films oriented in the direction of elongation have a higher tension, whereas the other directions exhibit lower tensions.

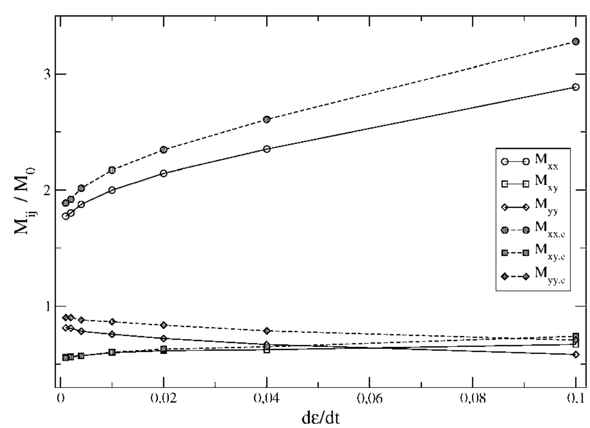

Fig. 9 Component of the symmetrical tensor M, built on the links between bubble centers or on the bubble edges (subscript e). They are rescaled respectively by $A/\sqrt{3}$ and $A/(3\sqrt{3})$.

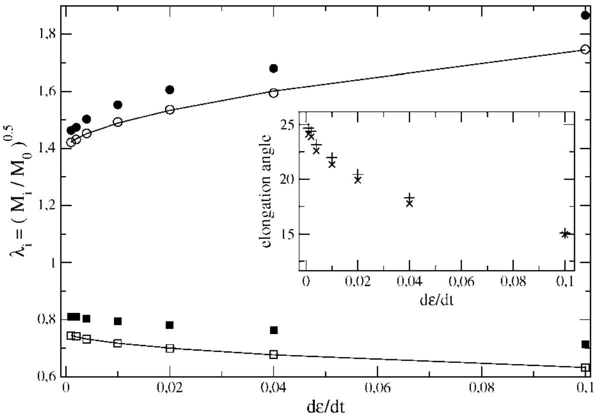

Fig. 10 Square root of the eigenvalues of the tensor M (open symbols) and M_e (full symbols), rescaled by the corresponding honeycomb values. The lines are the best power law fits. Inset: angle θ_1 between the x direction and the direction of the highest elongation eigenvector. +: M; ×: M_e.

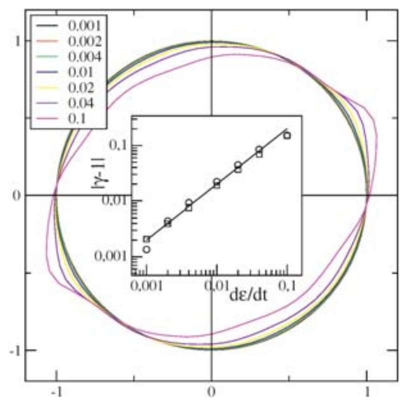

Fig. 11 Angular distribution of the edges tensions, for shear rates in the range $10^{-3} - 10^{-1}$. Inset: extremal tension variation $|\delta\gamma|$, in a log log plot. The straight line is $|\delta\gamma| = 2\dot{\varepsilon}$. ○ $\gamma_{max} - 1$; □ $1 - \gamma_{min}$. The data binning has been made with $\delta\theta = 5°$.

4.4 Foam plasticity

The T1 transformations are responsible for the foam plasticity. Fig. 12 shows that their number per bubble and per unit of deformation $dN_{T1}/d\varepsilon$ decreases with the shear rate. This can be directly related to the increase of bubble deformation. The foam structure evolution under simple shear can be seen as bubbles monolayers (oriented in the x direction) sliding over each other. When each layer has slid from one bubble size $\sqrt{M_{xx}}$ in the x direction, each bubble has got in average two new neighbors and has lost two, which corresponds to one T1 per bubble. As the layer thickness is $\sqrt{M_{yy}}$, the corresponding strain is $\varepsilon = \sqrt{M_{xx}}/\sqrt{M_{yy}}$, leading to $dN_{T1}/d\varepsilon = \sqrt{M_{yy}/M_{xx}}$. This rough estimate is verified numerically within 10%, without any numerical prefactor (see Fig. 12).

5 Discussion

The foam deformation and the tensions obtained numerically, and especially their dependency with the shear rate, proved to be

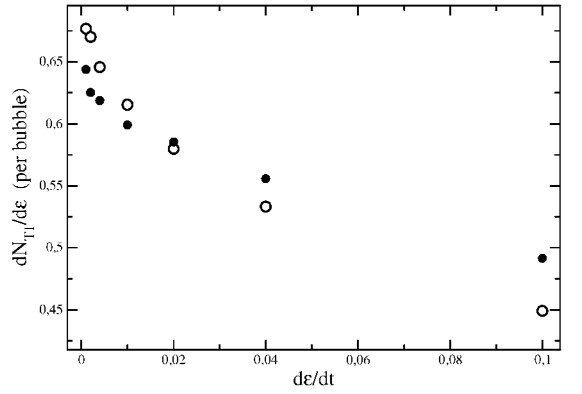

Fig. 12 Number of T1 per bubble and per unit deformation in the steady regime, as a function of the shear rate. ●: numerical result; ○: numerical value of $(M_{yy}/M_{xx})^{0.5}$.

difficult to rationalize using simple analytical laws. Simple local analysis, at the bubble scale, are derived in this section, trying to relate to each other the various quantities obtained numerically. This provides reference values that can be compared to numerical ones. The relatively poor agreement we obtain underlines the important role of the correlations, of the non-affine bubble motions and of the complex collective effects.

5.1 Maximal edge tensions

The tension obtained for a local steady elongation $\dot{\varepsilon}_{loc}$ is, at first order, $\gamma = 1 + \dot{\varepsilon}_{loc}$ (see eqn (5) with $\alpha = 1$). The extremal values of the tensions (for a data binning made with $\delta\theta = 5°$) are presented in the inset of Fig. 11. They are adjusted by the linear laws $\gamma_{min} \approx 1 - \varepsilon$ and $\gamma_{max} \approx 1 + 2\varepsilon$. The local elongation rate of a segment oriented in the direction θ relatively to the shear direction is, for an affine deformation at a shear rate $\dot{\varepsilon}$, $\dot{\varepsilon}_{loc} = \dot{\varepsilon}\sin\theta\cos\theta$, of the order of $0.3\dot{\varepsilon}$ for $\theta \approx 20°$. The average local elongation rate is thus much higher than the value corresponding to an affine deformation. Indeed, high elongation/contraction rates appear during the relaxation process after the T1.

5.2 Maximal bubble elongation

The tension difference between the three edges meeting at a vertex is partly responsible for the higher bubble elongation at higher shear rate. A rough estimate of the expected elongation, based on a local analysis on a hexagonal bubble, is given below. Using the simplified geometry shown on Fig. 13, we deduce the angle ϕ from the force balance $\gamma^+ = 2\gamma^- \cos\phi$, with $\gamma^+ = 1 + \delta\gamma$ the tension of the elongating edges l^+ and $\gamma^- = 1 - \delta\gamma$ the tension of the contracting edges l^-. The bubble area is given by

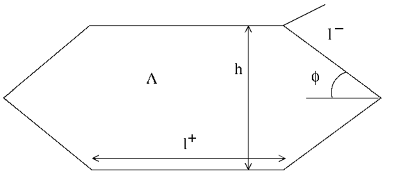

Fig. 13 Schematical bubble shape.

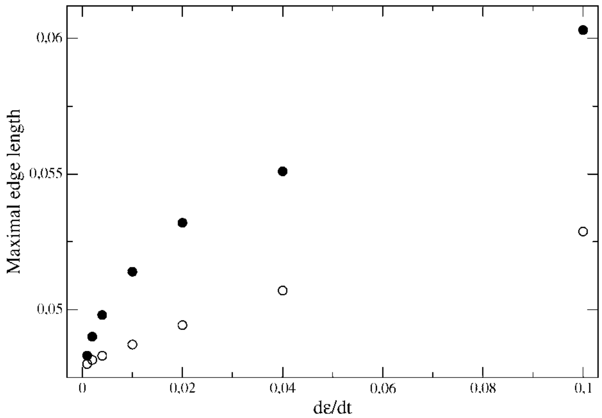

Fig. 14 ●: Average edge length in the most elongated direction (same data as Fig. 7, inset). ○: Prediction of eqn (14), using the numerical value of $\gamma_{max} - 1$ for $\delta\gamma$ (data from Fig. 11, inset).

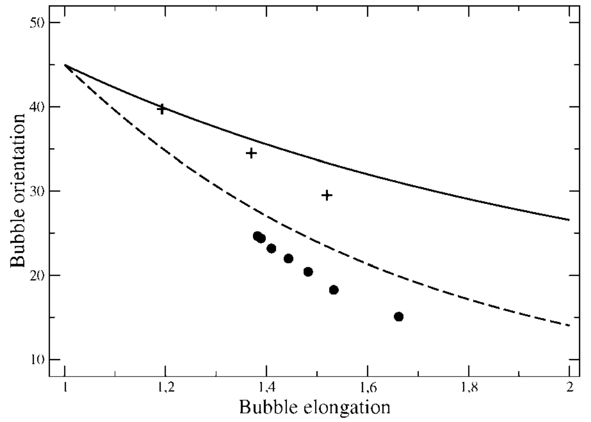

Fig. 15 Orientation θ_1 of the bubbles as a function of their elongation $\lambda = (M_1/M_2)^{1/4}$. ●: in the steady plastic regime, for $\dot{\varepsilon} \in [0.001 - 0.1]$ (data from Fig. 10); +: in the elastic transient, for $\dot{\varepsilon} = 0.04$ and $\varepsilon = 0.25; 0.5; 1$. These data are compared to arctan$(1/\lambda)$ (full line, eqn (17)); and to arccos $\left(1/\sqrt{1+\lambda^{-1/4}}\right)$ (dashed line, eqn (15)).

$A = 2l^- \sin\phi l^+ + 2(l^-)^2\cos\phi\sin\phi$. At first order in $\delta\gamma$, we thus get a geometrical relation between A, l^+ and l^-:

$$l^+ = \frac{A}{\sqrt{3}l^-}\left(1 + \frac{2\delta\gamma}{3}\right) - l^-\left(\delta\gamma + \frac{1}{2}\right) \quad (14)$$

This relation can be directly compared with the numerical data extracted from Fig. 7 and Fig. 11. As the orientation of the minimal edge length corresponds to a minimum of edges density and is thus not representative, we choose to determine l^-_{min} by setting in eqn (14) the quasi static values of $l_{max}{}^+$ and $\delta\gamma$ obtained numerically: $l^+_{max} = 0.05$ (see Fig. 7) and $\delta\gamma = 0$. This leads to $l^-_{min} = 0.016$ (of the same order of magnitude as $\varepsilon_l = 0.0036$ the numerical minimal edge value before a T1). Assuming that this minimal value l^-_{min} does not change with $\dot{\varepsilon}$, eqn (14) provides a rough prediction, only based on local arguments, of the increase of the maximal edge elongation with increasing shear rate. This estimate is plotted on Fig. 14 and compared with the numerical data. The value of $\delta\gamma$ used for each $\dot{\varepsilon}$ is given on Fig. 11 (inset).

This simple approach gives the right tendency, but does not allow to fully reproduce the numerical data. The predicted elongation increase $\delta l_{max}(\delta\gamma)$ is only a third of the value obtained numerically. More importantly, the edge elongation has a sub-linear behavior with the shear rate, whereas the tension increases roughly linearly with $\dot{\varepsilon}$. This is not compatible with the relation we obtain between tension and elongation, eqn (14) (this is a linearized expression, but higher order terms lead to the wrong concavity). The increase of the orientational order probably plays an important role and involves processes at a scale larger than the individual bubble scale.

5.3 Orientation of the elongated edges

Another interesting quantity is the orientation of the bubbles. At the very beginning of the deformation, bubbles are elongated in the direction $\theta = \pi/4$. For affine deformations of finite amplitude, the relation between the orientation of the most elongated direction θ and the elongation λ is given by the eqn (17), in appendix. The Fig. 15 represents the direction θ_1 of the eigenvector associated to λ_1, as a function of the elongation $\lambda = (\lambda_1/\lambda_2)^{1/2}$. The values obtained numerically are in agreement with the affine prediction at the beginning of the elastic regime and are slightly smaller at the end of the transient.

In the steady plastic regime, the bubbles are much more tilted. Raufaste *et al.* predicted that the relation 17 between orientation and elongation does not remain valid in the plastic regime and they establish another law for a purely elasto-plastic material:[27]

$$\cos\theta_1 = \frac{1}{\sqrt{1+\lambda^{-1/4}}} \quad (15)$$

This relation is plotted on Fig. 15 and predicts a smaller angle than in the elastic regime (at fixed elongation), in agreement with our numerical observations. This theory provides a much better estimation of our numerical results than the affine law, even if it predicts slightly too large angles. Here again, the role of the viscous dissipation is thus mainly to modify the yield elongation λ. The bubble orientation obtained at a shear rate $\dot{\varepsilon}$ with our non quasistatic model is close to the bubble orientation obtained with a purely elasto plastic model, with a yield strain equals to $\lambda(\dot{\varepsilon})$.

6 Conclusion

This paper proposes a new numerical technique to deal with the difficult question of dissipative processes and non equilibrium surface tensions in sheared liquid foams. Extensive results are given for a 2D foam under simple shear. We show that the stress obeys a Herschel–Bulkley law, with $n \approx 0.6$ and that the stress increase with increasing shear rate is mainly due to increasing bubble elongation that can be interpreted as an increase of the plastic threshold. We show that the number of T1 is related to the bubble elongation and that it decreases with increasing shear rate. This work provides new insights into the coupling between the local dissipation in films and the visco elasto-plastic response of the foam at the sample scale.

7 Appendix

The identity between a shear deformation in the x direction of amplitude ε and the transformation made of (i) a rotation of angle $-\theta'$, (ii) an elongation λ in the x direction and (iii) the rotation of angle θ, is given by the relation

$$\begin{bmatrix} 1 & \varepsilon \\ 0 & 1 \end{bmatrix} = \begin{bmatrix} \cos\theta & -\sin\theta \\ \sin\theta & \cos\theta \end{bmatrix} \begin{bmatrix} \lambda & 0 \\ 0 & 1/\lambda \end{bmatrix} \begin{bmatrix} \cos\theta' & \sin\theta' \\ -\sin\theta' & \cos\theta' \end{bmatrix} \quad (16)$$

where

$$\tan(2\theta) = 2/\varepsilon;\ \lambda = 1/\tan(\theta);\ \theta' = \pi/2 - \theta \quad (17)$$

If this transformation is made on an initially isotropic medium, the first rotation of angle $-\theta'$ does not play any role and the direction of largest elongation, for a shear amplitude ε, is simply θ, between $\pi/4$ for small ε and 0 for $\varepsilon \rightarrow \infty$.

Acknowledgements

This project was supported by the Institut Universitaire de France. We thank S. Cox and C. Raufaste for enlightening discussions.

References

1 R. Höhler and S. Cohen-Addad, *J. Phys.: Condens. Matter*, 2005, **17**, R1041.
2 P. Marmottant and F. Graner, *Eur. Phys. J. E*, 2007, **23**, 337.
3 S. Benito, C.-H. Bruneau, T. Colin, C. Gay and F. Molino, *Eur. Phys. J. E*, 2008, **25**, 225.
4 S. A. Khan, C. A. Schnepper and R. C. Amstrong, *J. Rheol.*, 1988, **95**, 69.
5 H. M. Princen and A. D. Kiss, *J. Colloid Interface Sci.*, 1989, **128**, 176.
6 A. D. Gopal and D. J. Durian, *J. Colloid Interface Sci.*, 1999, **213**, 169.
7 N. D. Denkov, V. Subramanian, D. Gurovich and A. Lips, *Colloids Surf., A*, 2005, **263**, 129.
8 P. Sollich, F. Lequeux, P. Hébraud and M. E. Cates, *Phys. Rev. Lett.*, 1997, **78**, 2020.
9 P. Sollich, *Phys. Rev. E: Stat. Phys., Plasmas, Fluids, Relat. Interdiscip. Top.*, 1998, **58**, 738.
10 P. Hébraud and F. Lequeux, *Phys. Rev. Lett.*, 1998, **81**, 2934.
11 L. Bocquet, A. Colin and A. Ajdari, *Phys. Rev. Lett.*, 2009, **103**, 036001.
12 N. D. Denkov, S. Tcholakova, K. Golemanov, K. P. Ananthapadmanabhan and A. Lips, *Phys. Rev. Lett.*, 2008, **100**, 138301.
13 N. D. Denkov, S. Tcholakova, K. Golemanov, K. P. Ananthpadmanabhan and A. Lips, *Soft Matter*, 2009, **5**, 3389.
14 G. Katgert, M. E. Möbius and M. van Hecke, *Phys. Rev. Lett.*, 2008, **101**, 058301.
15 C. Pozrikidis, *J. Eng. Math.*, 2001, **41**, 237.
16 A. M. Kraynik, *Annu. Rev. Fluid Mech.*, 1988, **20**, 325.
17 V. Langlois, S. Hutzler and D. Weaire, *Phys. Rev. E: Stat., Nonlinear, Soft Matter Phys.*, 2008, **78**, 021401.
18 D. Buzza, C.-Y. Lu and M. E. Cates, *J. Phys. II*, 1995, **5**, 37.
19 M. Durand and H. Stone, *Phys. Rev. Lett.*, 2006, **97**, 226101.
20 I. Cantat and R. Delannay, *Eur. Phys. J. E*, 2005, **18**, 55.
21 T. Okuzono and K. Kawasaki, *Phys. Rev. E: Stat. Phys., Plasmas, Fluids, Relat. Interdiscip. Top.*, 1995, **51**, 1246.
22 C. Raufaste, B. Dollet, S. Cox, Y. Jiang and F. Graner, *Eur. Phys. J. E*, 2007, **23**, 217.
23 A. M. Kraynik, D. A. Reinelt and H. M. Princen, *J. Rheol.*, 1991, **35**, 1235.
24 S. J. Cox and E. L. Whittick, *Eur. Phys. J. E*, 2006, **21**, 49.
25 T. E. Green, P. Grassia, L. Lue and B. Embley, *Colloids Surf., A*, 2009, **348**, 49.
26 D. Weaire, J. D. Barry and S. Hutzler, *J. Phys.: Condens. Matter*, 2010, **22**, 193101.
27 C. Raufaste, S. J. Cox, P. Marmottant and F. Graner, *Phys. Rev. E: Stat., Nonlinear, Soft Matter Phys.*, 2010, **81**, 031404.
28 F. Graner, B. Dollet, C. Raufaste and P. Marmottant, *Eur. Phys. J. E*, 2008, **25**, 349.

